International Journal of Heat and Fluid Flow 29 (2008) 1436–1446

Contents lists available at ScienceDirect

International Journal of Heat and Fluid Flow

journal homepage: www.elsevier.com/locate/ijhff

Simulation of liquid transfer between separating walls for modeling micro-gravure-offset printing

Wei-Xi Huang [a], Seung-Hyun Lee [a], Hyung Jin Sung [a,*], Taik-Min Lee [b], Dong-Soo Kim [b]

[a] Department of Mechanical Engineering, Korea Advanced Institute of Science and Technology, 373-1, Guseong-dong, Yuseong-gu, Daejeon 305-701, Republic of Korea
[b] Intelligence and Precision Machinery Research Division, Korea Institute of Machinery and Materials, 171, Jang-dong, Yuseong-gu, Daejeon 305-343, Republic of Korea

ARTICLE INFO

Article history:
Received 19 February 2008
Received in revised form 30 May 2008
Accepted 4 July 2008
Available online 26 August 2008

Keywords:
Micro-gravure-offset printing
Liquid transfer
Numerical simulation
Free-surface flow
Contact angle
Surface tension

ABSTRACT

A numerical study of the liquid transfer processes that occur during micro-gravure-offset printing is carried out. Specifically, liquid transfer between two parallel separating plates and between a trapezoidal cavity and an upward moving plate are simulated, as models of the printing of ink from the offset pad onto the substrate and the picking up of ink from the gravure plate by the offset pad, respectively. During the liquid transfer between two parallel plates, the stretching, breaking and recoil of the liquid are illustrated, and the generation of a satellite droplet is observed. The influences of the separation velocity, liquid viscosity, surface tension, gravity force, and contact angles on the liquid transfer are estimated. For the transfer of liquid from the cavity to the upward moving plate, the findings indicate that the process can be divided into three stages: (1) a whole stretching stage; (2) a central stretching, breakup and recoil stage; and (3) an equilibrium stage. The final width of transferred liquid is closely related to the contact angle at the upper plate, while the cut height is mainly affected by the contact angle at the cavity side wall. The effects of the initial distance and cavity shape are also discussed.

© 2008 Elsevier Inc. All rights reserved.

1. Introduction

The gravure-offset printing technique, which has traditionally been used in the graphic printing industry to produce items such as magazine covers and newspaper supplements (Gillett et al., 1991), has recently received much attention as a potential method for the cost-effective mass-production of micro-scale electrical circuits (Pudas, 2004). In gravure-offset printing, ink from an ink fountain is first poured into the grooves of the gravure plate or roller, and then excess ink is removed using a doctor blade. The ink in the grooves is then picked up by a silicone rubber roller. Finally, the roller is rotated over the target substrate, thereby transferring the ink from the roller to the substrate. In some situations, such as printing on non-planar surfaces, the silicone rubber roller is replaced by a soft pad that moves vertically to transfer the ink to the surface. Using a gravure plate and an offset pad as an example, a schematic of the above three-step ink transfer process is shown in Fig. 1.

Various experimental studies have shown that gravure-offset printing can be used to print narrow conductor lines with widths on the order of micrometers (Mikami et al., 1994; Lahti et al., 1999; Hagberg et al., 2001). However, the ink transfer efficiency and print quality are affected by many factors, such as material surface factors and ink factors (Elsayad et al., 2002; Pudas et al., 2004). Compared with experiment, numerical modeling provides a more convenient and economic way to test the effects of certain physical parameters, such as ink viscosity and surface properties (hydrophilic or hydrophobic), and geometrical parameters such as groove cavity shape and size. More importantly, numerical simulations can be used to study in detail the fundamental fluid dynamics of the ink transfer process, which is hard to observe or measure quantitatively in experiments.

Despite the potential advantages of numerical simulation over experiment, few numerical studies have been performed on the micro-gravure-offset printing process or related problems. Darhuber et al. (2000) carried out numerical simulations using the Surface Evolver software (Brakke, 1992), which takes into account the liquid's surface tension and the liquid–solid contact energy. Steepest descent and conjugate gradient methods were implemented for minimization of the total energy. Two numerical examples were presented: the equilibrium shape of the ink meniscus between two parallel plates, and the equilibrium shape of the ink meniscus between the stamp and the target substrate when a small tilt of 2° is present. It should be noted that their simulations assumed quasistatic printing and unconstrained contact line motion; hence, the results were only affected by the surface contact angle, regardless of the properties of the ink. Powell et al. (2002) developed a Lagrangian finite element algorithm to solve time-dependent free surface flows. They first simulated stretching of a viscous liquid filament between two flat plates. In these simula-

* Corresponding author. Tel.: +82 42 350 3027; fax: +82 42 350 5027.
E-mail address: hjsung@kaist.ac.kr (H.J. Sung).

0142-727X/$ - see front matter © 2008 Elsevier Inc. All rights reserved.
doi:10.1016/j.ijheatfluidflow.2008.07.002

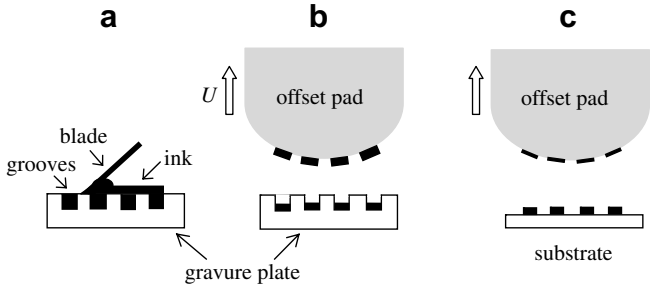

Fig. 1. Schematics of gravure-offset printing: (a) filling ink into the grooves; (b) picking up ink by the offset pad; (c) printing ink on the substrate.

tions, the liquid underwent considerable deformation and the simulation was stopped when the filament became thinner than a certain threshold thickness. The second example was a Newtonian liquid pulled from a two-dimensional upturned trapezoidal cavity by a downward moving plate. These simulations assumed perfect adherence between the liquid and the moving plate on which there are two 'static' contact lines, but permitted local slip between the liquid and the trapezoidal cavity walls at the dynamic contact lines. Moreover, a simplified physical model of liquid withdrawal from gravure cavities was proposed by Schwartz et al. (1998) and Schwartz (2002) based on a lubrication model. Three-dimensional unsteady liquid motion was simulated for a system in which the flow domain was bounded above by a stress-free surface and below by a moving substrate. Recently, Yin and Kumar (2005) studied the flow between a cavity and a flexible wall using a 1D lubrication model. In their model, the liquid flow is governed by the Reynolds equation, while the flexible wall is linked to its equilibrium position by Hookean springs and/or held by a uniform tension force.

In direct numerical simulations of the Navier–Stokes (N–S) equations, the free surface between ink and ambient air can be tackled by two techniques. One approach is the aforementioned Lagrangian finite element method (Powell et al., 2002), which has also been used to simulate the liquid drop formation process typically seen in ink-jet printing (Wilkes et al., 1999). In this method, the grid is made to conform to the free surface and is stretched as the liquid drop or filament is deformed. To achieve this, a structured remeshing is needed at every time step and the computation has to be stopped at a certain threshold thickness of the ink filament before breakup. The other approach is the volume of fluid (VOF) method, in which the full N–S equations are solved by finite difference discretization on an Eulerian grid (Hirt and Nichols, 1981). Thus, in this method the free surface can move through the grid, making it capable of handling the breakup of the liquid filament. Although the free surface is smeared over several grid cells, the accuracy of this method has been demonstrated in various studies (Scardovelli and Zaleski, 1999). Zhang (1999) showed that numerical simulations of drop formation using the VOF method were in good agreement with experimental results. In their simulations, they studied the breakup process of the liquid filament and the subsequent generation of satellite droplets. In the present work, we employ the VOF method to simulate the liquid transfer process that occurs in micro-gravure-offset printing. In the next section we introduce the problem formulation and numerical method. Numerical results are presented in Section 3, and a summary is given in Section 4.

2. Problem formulation and numerical method

For computational purposes, we consider ink transfer within a simpler geometry than in the real micro-gravure-offset printing process, as shown in Fig. 2. Fig. 2a shows the configuration for ink transfer between a trapezoidal cavity and a moving plate, representing the second step in the printing process at which the ink is picked up by the offset pad from the grooves in the gravure plate (Fig. 1b), and Fig. 2b shows the configuration for ink transfer between two parallel separating plates, corresponding to the third step of the printing process at which ink is applied to the substrate (Fig. 1c). The rationale underlying the simplifications made in the present computational model is that the soft pad is initially pressed tightly toward the gravure plate or the target substrate, and the groove sizes are very small. Even for the offset roller, the width of the contact area at the impression nip, although dependent on rubber hardness and imprint pressure, is usually much larger than the groove sizes (Gillett et al., 1991).

The fluid flow in the present model contains both liquid and gas phases, and has a moving boundary. For convenience, an integral form of the governing equations is used to describe the fluid motion. Specifically, for an arbitrary control volume V with a closed surface S (e.g. a computational cell), the equations for the conservation of mass and momentum are written as follows, respectively:

$$\frac{\partial}{\partial t}\int_V \rho \mathrm{d}V + \oint_S \rho(\boldsymbol{u}-\boldsymbol{u}_g)\cdot\boldsymbol{n}\mathrm{d}S = 0, \tag{1}$$

$$\frac{\partial}{\partial t}\int_V \rho\boldsymbol{u}\mathrm{d}V + \oint_S \rho\boldsymbol{u}(\boldsymbol{u}-\boldsymbol{u}_g)\cdot\boldsymbol{n}\mathrm{d}S = \oint_S \boldsymbol{\tau}\cdot\boldsymbol{n}\mathrm{d}S + \int_V(\rho\boldsymbol{g}+\boldsymbol{f})\mathrm{d}V, \tag{2}$$

where ρ is the density, $\boldsymbol{u} = (u,v)$ is the velocity vector, $\boldsymbol{u}_g$ is the velocity of the control volume surface S with its unit normal vector denoted by $\boldsymbol{n}$, $\boldsymbol{\tau}$ is the stress tensor, $\boldsymbol{g}$ is the gravity force, and $\boldsymbol{f}$ is the surface tension force. For an incompressible flow, the stress tensor is defined by $\boldsymbol{\tau} = -p\boldsymbol{I} + \mu[\nabla\boldsymbol{u} + (\nabla\boldsymbol{u})^{\mathrm{T}}]$, where p is the pressure, μ is the dynamic viscosity, and $\boldsymbol{I}$ is the unit tensor. Since the system of interest contains free surfaces, the VOF method is used. Thus, a liquid volume fraction ϕ is defined by

$$\phi = \begin{cases} 1, \text{inside the liquid phase;} \\ >0, <1, \text{at the free surface;} \\ 0, \text{inside the gas phase.} \end{cases} \tag{3}$$

The position of the free surface can be determined by the passive transport equation (Hirt and Nichols, 1981)

$$\frac{\partial\phi}{\partial t} + \boldsymbol{u}\cdot\nabla\phi = 0, \tag{4}$$

which can also be written in the integral form by making use of $\nabla\cdot\boldsymbol{u} = 0$, as follows

$$\frac{\partial}{\partial t}\int_V \phi\mathrm{d}V + \oint_S \phi(\boldsymbol{u}-\boldsymbol{u}_g)\cdot\boldsymbol{n}\mathrm{d}S = 0. \tag{5}$$

Then the shape of the free surface is reconstructed by the second-order piecewise linear interface construction (PLIC) scheme (Rider and Kothe, 1998). For computational cells containing the free surface, the density ρ and the dynamic viscosity μ are calculated based on the volume fraction ϕ,

$$\rho = \phi\rho_l + (1-\phi)\rho_g, \tag{6}$$

$$\mu = \phi\mu_l + (1-\phi)\mu_g. \tag{7}$$

In the above Eqs. (6) and (7), the subscripts 'l' and 'g' denote the liquid and gas phases, respectively. The surface tension force is expressed by

$$\boldsymbol{f} = \sigma\kappa\boldsymbol{n}_s, \tag{8}$$

where σ denotes the surface tension coefficient, κ denotes the local free surface curvature, and $\boldsymbol{n}_s = \nabla\phi/|\nabla\phi|$ denotes the unit normal vector of the free surface. The local curvature κ can be calculated from $\kappa = -(\nabla_s\cdot\boldsymbol{n}_s)$, where ∇_s denotes the gradient operator applied

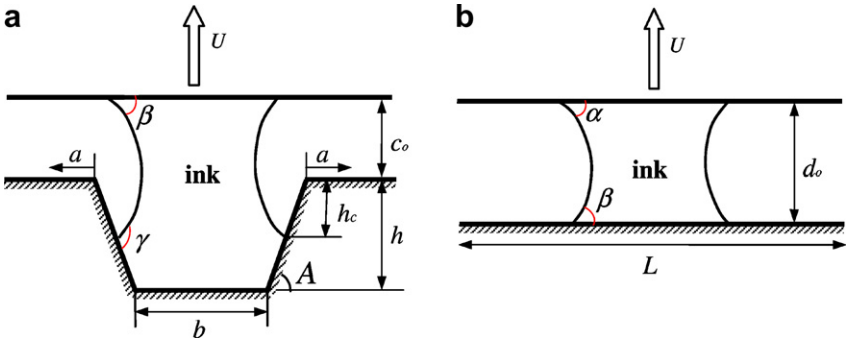

Fig. 2. Computational geometrical configurations of ink transfer between (a) a trapezoidal cavity and a plate and (b) two parallel plates.

along the direction tangent to the surface, as derived by Brackbill et al. (1992).

The no-slip boundary condition is applied at the top and bottom walls, and the left and right edges are treated as outlets where a fixed pressure is given. In the computation, a symmetric boundary condition is used at the center line to reduce the grid size by 50% due to the symmetry of the system. At the solid boundary, a contact line (see Fig. 2) is formed where the free surface meets the wall. Although the no-slip condition is applied in solving the governing equations (Eqs. (1), (2), and (5)), the contact line is allowed to move freely on the wall and the contact angle is kept constant in the reconstruction of the free surface. In the present simulation, the lower wall (plate or cavity) is fixed, while the upper wall is moving vertically, as shown in Fig. 2. Thus, a grid deformation is required at each time step. As an example, Fig. 3 shows both the initial and final stages of the computational grid system between a cavity and a plate; it is clear that the grid is stretched by the moving plate. The grid velocity at a particular instant is obtained from the grid positions at two consecutive time steps.

The above governing equations, together with the boundary conditions, are discretized by the finite volume method using a collocated grid system. The pressure–velocity coupling is tackled using the SIMPLEC algorithm (Van Doormaal and Raithby, 1984). The checkerboard problem is circumvented by relating the velocity at the cell interface directly to the local pressure gradient (Pericc et al., 1988). A second-order upwind scheme is used to evaluate the fluxes at the cell interface. The gravity force and the surface tension force are included in the source term. The explicit Euler scheme for time advancement is employed for the transport equation of ϕ and the momentum equations. The resulting system of algebraic equations is then solved directly or iteratively at each time step.

3. Results

3.1. Liquid transfer between two parallel plates

To facilitate comparison with previous studies (Darhuber et al., 2000; Powell et al., 2002), we regard the upper plate as the target substrate in Fig. 2b, which is equivalent to moving the upper offset pad and fixing the lower substrate (Fig. 1c) according to relative motion. The parameters used in the present simulation are listed in Table 1. The same parameters are selected in the following unless otherwise stated.

3.1.1. A liquid drop on a stationary plate

First we consider a liquid drop on a stationary plate, which corresponds to the state before liquid transfer. Initially a drop of rectangular shape is placed on the lower plate but detached from the upper plate. Due to the surface tension, the drop takes on a circular shape in the absence of gravity in order to minimize its surface area. As shown in Fig. 4, the surface becomes a circular arc for $\beta = 45°$ and a half circle for $\beta = 90°$. The width and height of the liquid drop, denoted by w_o and h_o, respectively, can be simply derived from the surface geometry,

$$w_o = 2\sin\beta\sqrt{V_o/(\beta - \sin\beta\cos\beta)}, \tag{9}$$

$$h_o = (1 - \cos\beta)\sqrt{V_o/(\beta - \sin\beta\cos\beta)}, \tag{10}$$

where V_o denotes the volume of the liquid. Here the angle in units of radians rather than degrees is used in Eqs. (9) and (10), as well as in the following equations. In our simulation, the width and height are estimated by summing the volume fraction ϕ along the appropriate directions. Thus, we can obtain definite values of the width and height, despite the fact that the free surface is not sharp in the numerical simulation. Fig. 5 shows the values obtained for w_o and

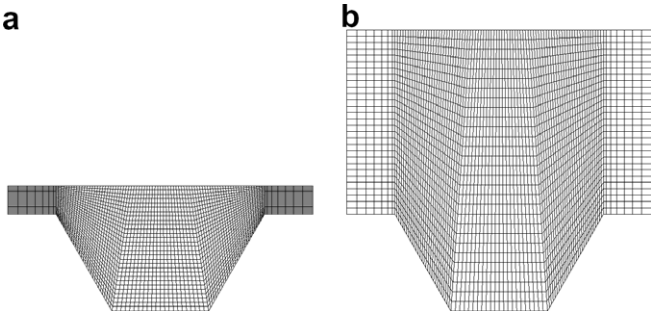

Fig. 3. Computational grid system between a cavity and a plate at (a) the initial stage and (b) the final stage.

Table 1
Parameters used in the simulation of liquid transfer between two parallel plates

Density of the liquid, ρ_l	1000 kg/m^3
Dynamic viscosity of the liquid, μ_l	0.1 N s/m^2
Surface tension coefficient, σ	1 N/m
Density of the surrounding air, ρ_g	1.16 kg/m^3
Dynamic viscosity of the air, μ_g	1.81×10^{-5} N s/m^2
Gravity acceleration, g	0
Separation speed, U	0.1 m/s
Plate length, L	20 μm
Volume of the liquid, V_o	32 μm^2
Initial distance between the two plates, d_o	8 μm
Grid number in the horizontal direction, N_x	21
Grid number in the normal direction, N_y	41
Computational time step, Δt	0.02 μs

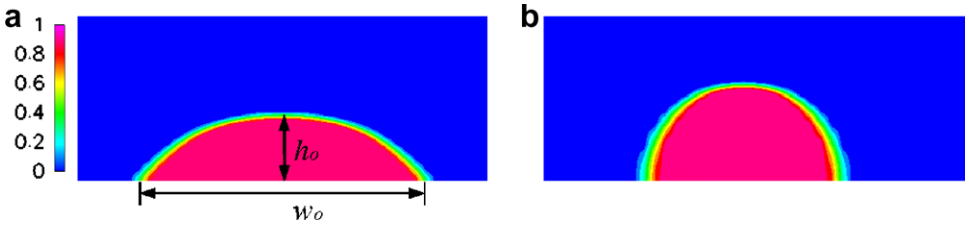

Fig. 4. Contour of the volume fraction of a liquid drop on a plate with a contact angle of (a) $\beta = 45°$ and (b) $\beta = 90°$. The same contour legend for density is used in the following. The width and height of the liquid drop are denoted by w_o and h_o, respectively.

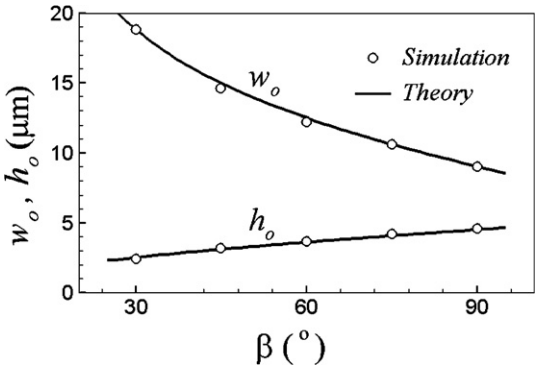

Fig. 5. Variations of the width and height of the liquid drop with the contact angle.

h_o as a function of β in the present numerical simulations, as well as the theoretical solutions (i.e. Eqs. (9) and (10), respectively). The simulation results are in good agreement with the theoretical curves.

3.1.2. Transfer process and parameter study

To simulate the liquid transfer induced by the upward movement of one plate, a liquid filament of rectangular shape is extended between the two plates, which are initially separated by a distance d_o. Before running the simulation with the moving plate, we equilibrate the system with a fixed the upper plate. During this preliminary step, the liquid filament is deformed due to its surface tension and converges to its lowest-energy shape, which is then used as the initial condition for the liquid transfer simulation. Fig. 6 shows the transfer process using instantaneous contours of

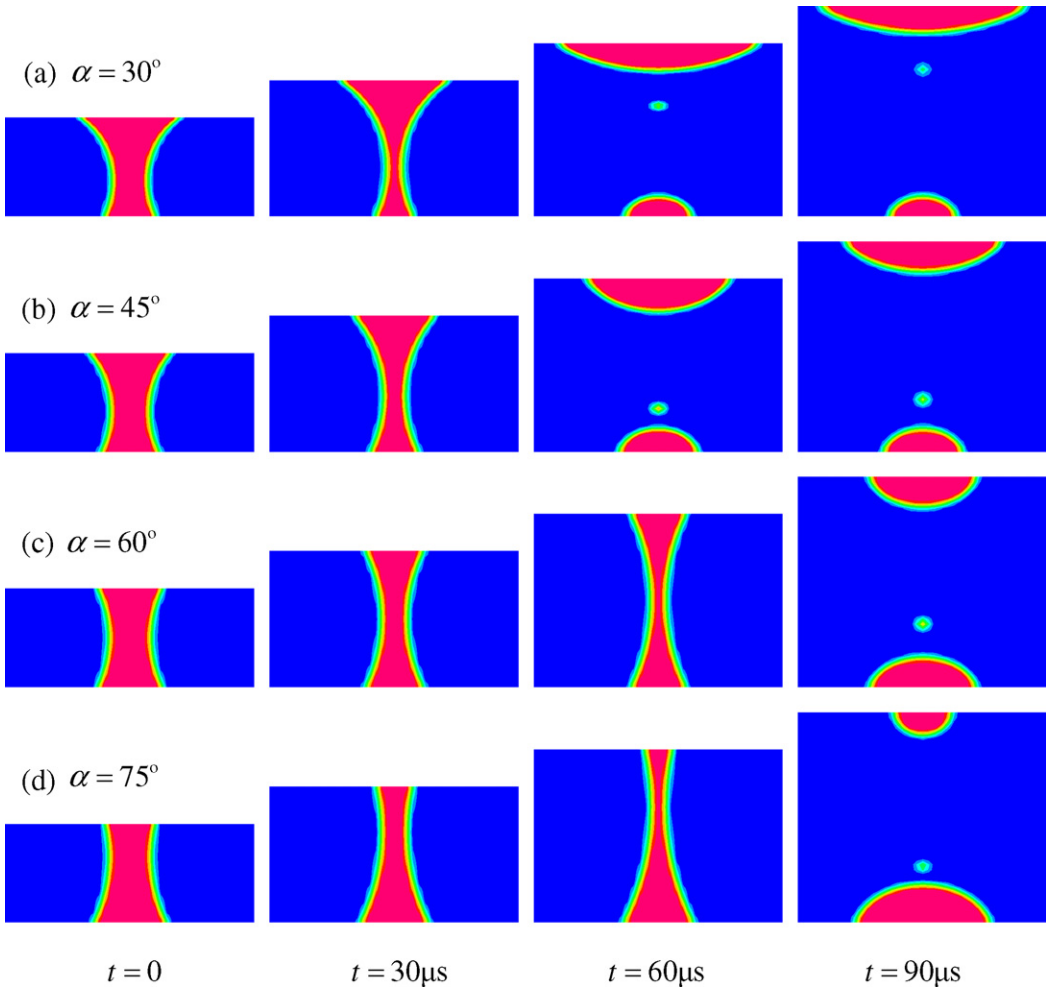

Fig. 6. Instantaneous contours of the volume fraction of the liquid between two parallel plates with $\beta = 60°$.

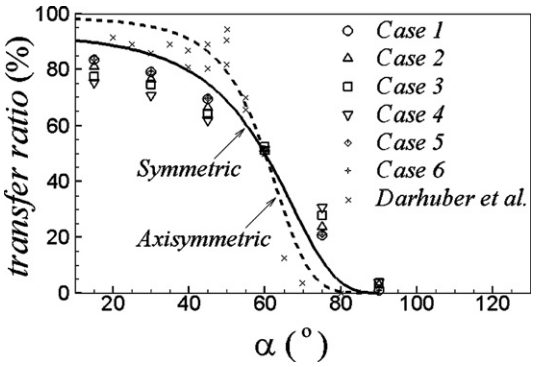

Fig. 7. Transfer ratio of the liquid between two parallel plates with $\beta = 60°$ as a function of α. The solid and dash lines denote the theoretical solutions under the quasistatic assumption for symmetric and axisymmetric geometries, respectively. Parameters for cases 1–6 are listed in Table 2.

the volume fraction ϕ for different α but constant β. Four time instants are shown for each case, i.e. $t = 0$, 30, 60 and 90 μs. As time progresses, the liquid filament is stretched by the upward moving plate, while the contact lines are moving simultaneously due to the surface tension. Finally the liquid filament is broken, and the computation is stopped when the liquid drops on both plates attain their equilibrium shapes. For $\alpha < \beta = 60°$ (Fig. 6a and b), more than half of the liquid is transferred to the upper plate. Exactly half of the liquid is transferred for $\alpha = \beta = 60°$ (Fig. 6c), and less than half for $\alpha > \beta = 60°$ (Fig. 6d). In addition, during the breakup process, a satellite droplet is generated. The formation of this droplet is similar to the behavior observed during drop formation from a nozzle or orifice (Zhang, 1999), which was found to be caused by the process of double breakage of the liquid filament (Peregrine et al., 1990).

Fig. 7 shows the final liquid transfer ratio for $\beta = 60°$ as a function of α. The liquid transfer ratio is high for small α but decreases rapidly when α is close to or larger than β. The system described above (designated as Case 1) uses the parameters provided in Table 1. We now consider further four cases (cases 2–6), in which we change the separation velocity U, the dynamic viscosity μ, the surface tension coefficient σ, the volume of liquid V_o and the gravity acceleration g individually, as listed in Table 2. The Reynolds number ($Re = \rho_l U\sqrt{V_o/2}/\mu_l$), the capillary number ($Ca = \mu_l U/\sigma$), and the Froude number ($Fr = g\sqrt{V_o/2}/U^2$) are also given in Table 2. From Fig. 7, we see that the final transfer ratio is decreased for $\alpha < \beta$ but increased for $\alpha > \beta$ as the capillary number Ca increases gradually from case 1 to case 4. Under the quasistatic assumption, the final transfer ratio is independent of the separation velocity and the liquid properties, and can be derived theoretically by

$$\mathrm{tr}\% = f(\alpha)/(f(\alpha) + f(\beta)) \times 100\%, \tag{11}$$

where the function

$$f(x) = \begin{cases} -\pi/4 + x/2 + \cos x - \sin x \cos x/2, & \text{symmetric} \\ -\pi/2 + x + 2\cos x - \sin x \cos x - (\cos x)^3/3, & \text{axisymmetric} \end{cases}, x = \alpha \text{ or } \beta$$

Table 2
Parameters used in the simulations of cases 1–6

	U (m/s)	μ (N s/m^2)	σ (N/s)	V_o (μm^2)	g (m/s^2)	Re	Ca	Fr
Case 1	0.1	0.1	1.0	32	0	0.004	0.01	0
Case 2	0.2	0.1	1.0	32	0	0.008	0.02	0
Case 3	0.1	0.5	1.0	32	0	0.0008	0.05	0
Case 4	0.1	0.1	0.1	32	0	0.004	0.1	0
Case5	0.1	0.1	1.0	3200	0	0.04	0.01	0
Case 6	0.1	0.1	1.0	32	10	0.004	0.01	0.004

is a factor of the liquid volume which can be obtained by using the property that the free surface has a circular shape. As shown in Fig. 7, the deviation of the numerical results from the quasistatic solution becomes larger as Ca increases. Data from Darhuber et al. (2000), which are also included in Fig. 7 for comparison, show the same tendency as the present data. The discrepancies between the two sets of data are not surprising given that Darhuber et al. adopted the axisymmetric condition and the quasistatic assumption in their simulations. In addition, the effects of the liquid size and the gravity force are negligible in cases 1, 5 and 6 in Fig. 7 since the Reynolds number and the Froude number are small for all the cases, indicating that the gravity force is much smaller than the inertial force and the inertial force is much smaller than the viscous force, which in turn is much smaller than the surface tension by considering also the capillary number (see Table 2).

Fig. 8 shows the time history of the minimum thickness of the liquid filament (w_m) during the transfer process. Here, α and β are chosen to be the same, so the minimum thickness is at the middle of the filament. The data show that for smaller α and β, the initial value w_m is smaller and decreases faster, since more liquid is attached to the plates and the mid part is thinner. Especially, for $\alpha = \beta = 90°$, the liquid filament always has a rectangular shape; thus a simple expression for w_m can be obtained as follows:

$$w_m = \frac{V_o}{d_o + Ut}. \tag{12}$$

In Fig. 8, the present numerical results are in excellent agreement with the theoretical expression (Eq. (12)) for $\alpha = \beta = 90°$.

The final width of the liquid transferred to the upper plate (w_t) is plotted in Fig. 9 for various α and β. From Fig. 9a, we can see that both α and β significantly influence w_t. As α increases or β decreases, w_t decreases monotonically. For $\alpha = \beta$, the transfer ratio is approximately 50%; hence w_t can be estimated from Eq. (9) by replacing V_o with $V_o/2$ and is equivalent to

$$w_t = w_o/\sqrt{2}. \tag{13}$$

The above relationship is plotted in Fig. 9b and shows good agreement with the numerical result of $\alpha = \beta$, indicating that the volume of the satellite droplet is negligible.

In the above simulations we consider only Newtonian liquids. However, in the printing of electronic circuitries, the conductor ink is non-Newtonian because it contains a low percent of solvent and a high concentration of solid particles, which results in a shear-thinning rheology (Pudas et al., 2002). Here we adopt the Carreau law to deal with the shear-thinning effect:

$$\mu_l = \mu_0(1 + (\lambda\dot{\varepsilon})^2)^{\frac{n-1}{2}}, \tag{14}$$

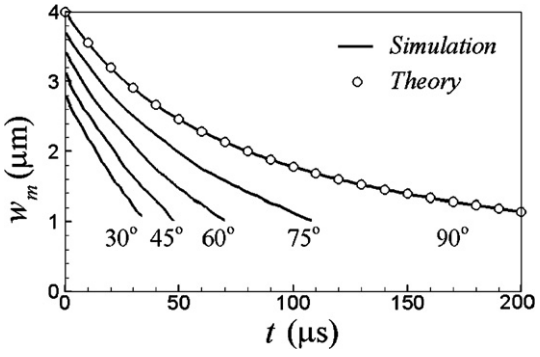

Fig. 8. The minimum thickness of the liquid filament during transfer process between two parallel plates with $\alpha = \beta = 30°$, 45°, 60°, 75° and 90°. The theoretical prediction is also shown for comparison.

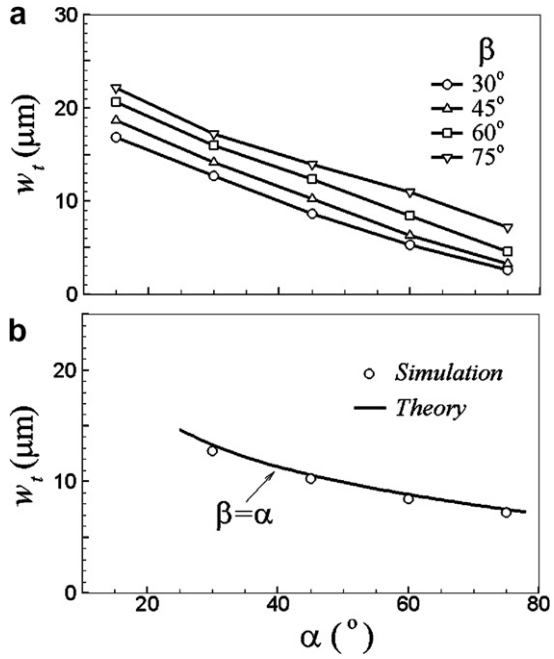

Fig. 9. Width of the liquid on the upper plate at the end of transfer as a function of α: (a) $\beta = 30°$, 45°, 60° and 75°; (b) $\beta = \alpha$.

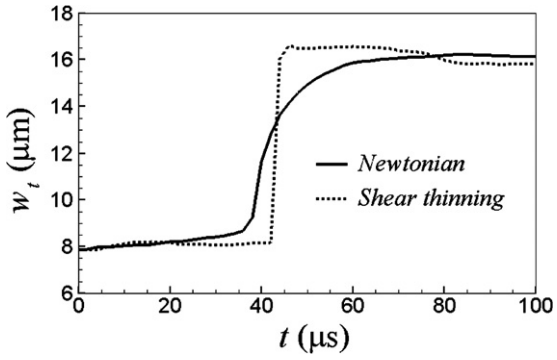

Fig. 10. Time histories of the width of liquid on the upper plate for Newtonian and shear-thinning liquids with $\alpha = 30°$ and $\beta = 60°$.

where μ_0, λ and n are material coefficients, and $\dot{\varepsilon} = \partial u/\partial y + \partial v/\partial x$ denotes the shear rate (Kennedy, 1995). In this simulation, we let $\mu_0 = 0.1$, $\lambda = 0.1$ and $n = 0.4$. Fig. 10 shows time histories of the width of the liquid on the upper plate (w_t) for both Newtonian and shear-thinning fluids with $\alpha = 30°$ and $\beta = 60°$. The main difference appears during the breakup process, where w_t is increased gradually for the Newtonian fluid but sharply for the shear-thinning fluid. Due to the small size of the present model and the large surface tension, a high shear rate is produced during the transfer process and causes a significant decrease of the viscosity. The instantaneous contours of the volume fraction ϕ near the breakup time are displayed in Fig. 11. We see after breakup that the Newtonian fluid is recoiled gradually toward the upper plate, while the shear-thinning fluid is attached to the upper plate immediately. In addition, more liquid droplets are generated for the shear-thinning fluid during this fast breakup process.

3.2. Liquid transfer between a cavity and a plate

In this case, the fluid properties and the separation velocity are chosen to be the same as those used in the simulations described above, as listed in Table 1. The gravity force is also neglected. The geometrical and computational parameters of the present model (Fig. 2a) are summarized in Table 3. In the following simulations, we may change one or two parameters in Table 3 for comparison as well as the contact angles, while the cavity opening width a is always kept the same. The Reynolds number defined by $Re = \rho_l U a/\mu_l$ is 0.01, and the capillary number $Ca = \mu_l U/\sigma$ is also 0.01 for this case.

3.2.1. Stationary liquid within the cavity

Similar to the previous section, we first calculated the stationary shape of the liquid within the cavity, as shown in Fig. 12. For this calculation, we set the initial liquid shape to be a trapezoid with a volume of $V_o = 32\ \mu m^2$, which corresponds to 90% of the cavity capacity. The shape of the liquid free surface is determined by the contact angle γ and the cavity incline angle A, which is 60° in the present simulation. The free surface is concave for $\gamma < A$ (Fig. 12a), perfectly flat for $\gamma = A$ (Fig. 12b), and convex for $\gamma > A$ (Fig. 12c and d). According to the geometrical relationship, the cen-

Table 3
Parameters used in the simulation of liquid transfer between a cavity and a plate

Cavity open width, a	10 μm
Cavity depth, h	5 μm
Cavity bottom width, b	4.23 μm
Cavity incline angle, A	60°
Volume of the liquid, V_o	32 μm^2
Initial distance between cavity and plate, c_o	1 μm
Grid number in the horizontal direction, N_x	81
Grid number in the normal direction, N_y	41
Computational time step, Δt	0.005 μs

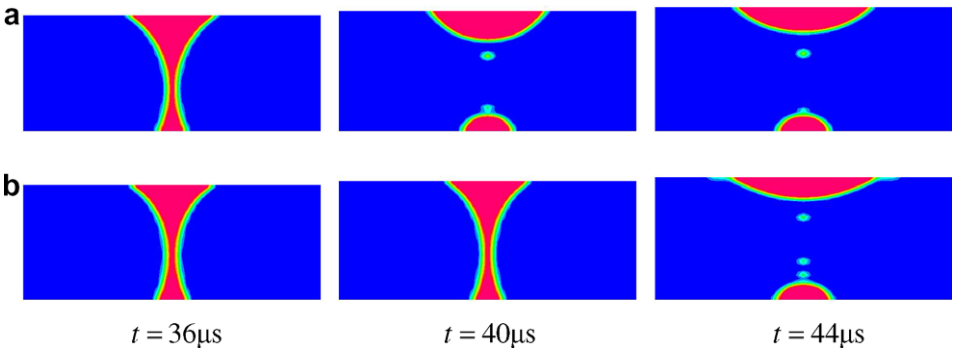

Fig. 11. Instantaneous contours of the volume fraction of the liquid between two parallel plates with $\alpha = 30°$ and $\beta = 60°$ for (a) Newtonian liquid and (b) shear-thinning liquid.

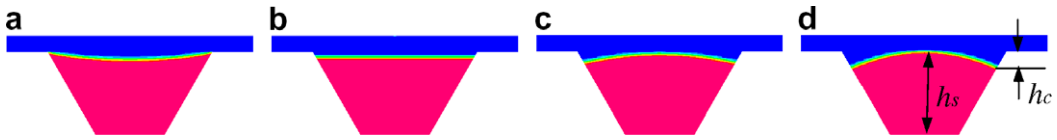

Fig. 12. Contour of the volume fraction of liquid in the cavity with a contact angle of (a) $\gamma = 45°$; (b) $\gamma = 60°$; (c) $\gamma = 75°$; (d) $\gamma = 90°$. The central height and the cut height are denoted by h_s and h_c, respectively.

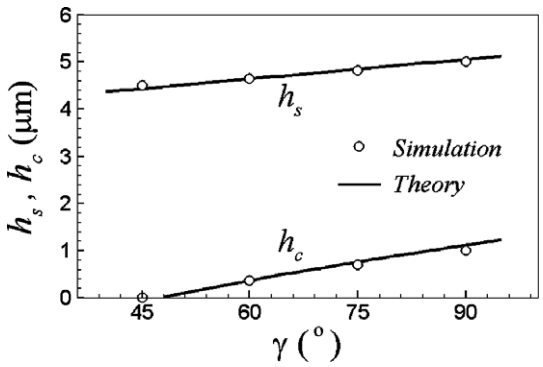

Fig. 13. Variations of the central height and the cut height of the liquid in the cavity with the contact angle.

tral height h_s and the cut height h_c of the liquid within the cavity, as marked in Fig. 12d, can be expressed as

$$h_s = h_a + x\sin A, \tag{15}$$

$$h_c = h - x\sin A, \tag{16}$$

where h_a denotes the arc height,

$$h_a = (b/2 + x\cos A)[1 - \cos(\gamma - A)]/\sin(\gamma - A), \tag{17}$$

and x is the positive root of the quadratic equation,

$$(b + x\cos A)x\sin A + (b/2 + x\cos A)^2 F = V_o, \tag{18}$$

with the coefficient $F = [(\gamma - A) - \sin(\gamma - A)\cos(\gamma - A)]/\sin^2(\gamma - A)$. Eqs. (15) and (16) are plotted in Fig. 13. We see that both the central height h_s and the cut height h_c increase as γ increases. For $\gamma < 45°$, h_c is zero since the contact line reaches the cavity upper corner. Good

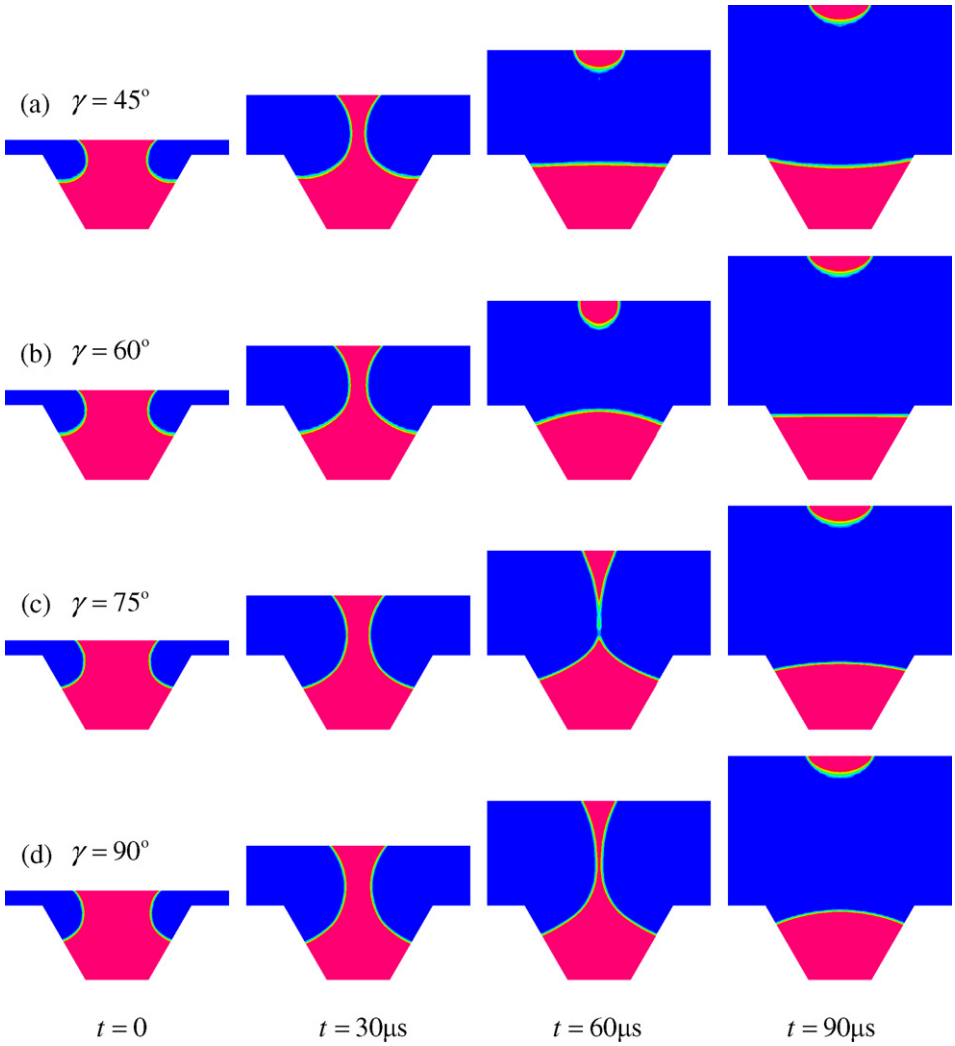

Fig. 14. Instantaneous contours of the volume fraction of the liquid between cavity and plate with $\beta = 60°$.

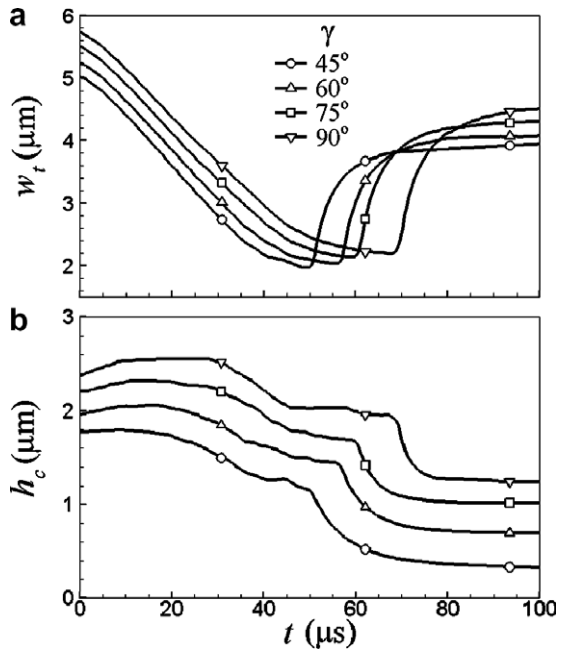

Fig. 15. Time histories of the width of liquid on the upper plate (a) and the cut height (b) with $\beta = 60°$ and different γ.

agreement between the present numerical results and the theoretical solutions is observed in Fig. 13.

3.2.2. Transfer process and effects of contact angles

Next, simulations of liquid transfer between the cavity and an upward moving plate are carried out. The initial position of the liquid free surface is obtained by iteration after the liquid with the same volume V_o is given attached to both the cavity and the upper plate. At the next step, the upper plate is set to move vertically at a speed of $U = 0.1$ m/s. The instantaneous contours of the volume fraction ϕ at four time instants, $t = 0$, 30, 60 and 90 μs, are shown in Fig. 14, where β is fixed at 60° but different γ values are selected for comparison. As the plate moves upward, the liquid filament is stretched until it breaks, after which the liquid recoils to the cavity and the plate by surface tension. As γ increases, the contact lines move deeper along the cavity side walls. Moreover, the breakup time is increased slightly for larger γ, but the ratio of transferred liquid is similar for all γ. It is observed that the contact line is difficult to move on the inclined cavity side wall by liquid stretching because a large surface tension force is required to compete with the inertial force of the liquid below the contact line. Hence the liquid within the cavity is similar to that on a flat plate with a small contact angle. As a result, the transfer process is weakly affected by γ and a satellite droplet is not generated in this case.

Fig. 15 shows time histories of the width of the liquid on the upper plate (w_t) and the cut height of the liquid on the cavity side wall (h_c). According to Fig. 15, the transfer process can be divided into three stages. In the first stage ($t < 40$ μs), w_t decreases gradually due to stretching, while h_c increases at the beginning and decreases after reaching its maximum. In the second stage (40 μs $< t < 80$ μs), w_t and h_c initially remain constant, indicating that the liquid filament is only stretched in its central part, but subsequently w_t increases and h_c decreases sharply due to recoil of the liquid after breakup. In the final stage ($t > 80$ μs), both w_t and h_c converge to their equilibrium values, and the transfer process is finished. At the end of the transfer process, w_t becomes slightly larger and h_c increases as γ increases.

The final w_t and the maximum h_c for different values of β and γ are collected in Fig. 16. As shown in Fig. 16a, the final w_t decreases as β increases, but the effect of γ is insignificant. In particular, when $\beta > 60°$, the final w_t is the same for all γ. On the contrary, the maximum h_c increases obviously with increasing γ, but decreases very slightly as β increases except in the vicinity of $\beta = 90°$ (see Fig. 16b). The displacement of the contact line on the cavity side wall has only a small effect on the fluid filament thickness during stretching, unlike the liquid transfer between two parallel plates. Hence the final w_t, as well as the liquid transfer ratio, depend only weakly on γ, although the maximum h_c varies with γ.

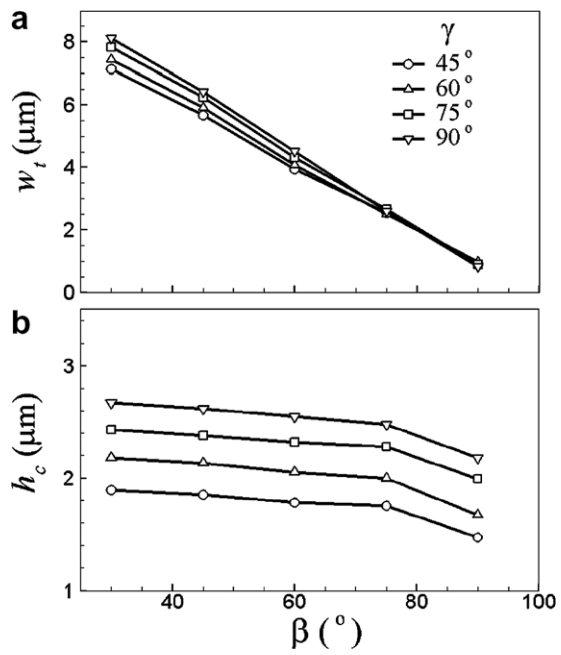

Fig. 16. Variations of the final width of liquid on the upper plate (a) and the maximum cut height (b) as functions of β and γ.

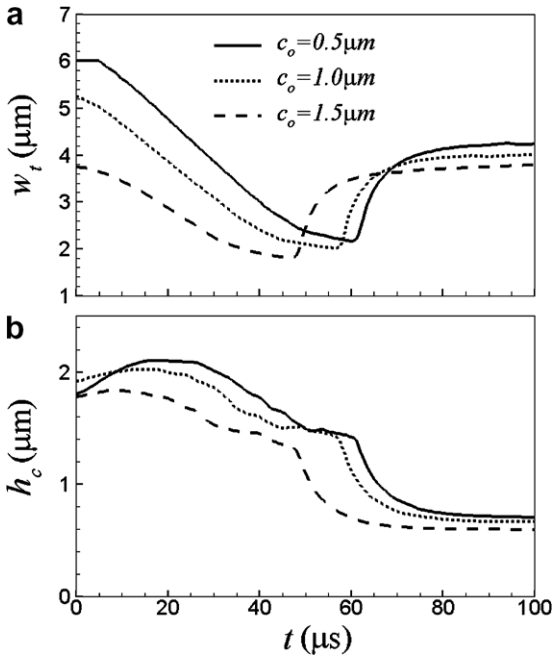

Fig. 17. Time histories of the width of liquid on the upper plate (a) and the cut height (b) with $\beta = \gamma = 60°$ for different initial distance c_o.

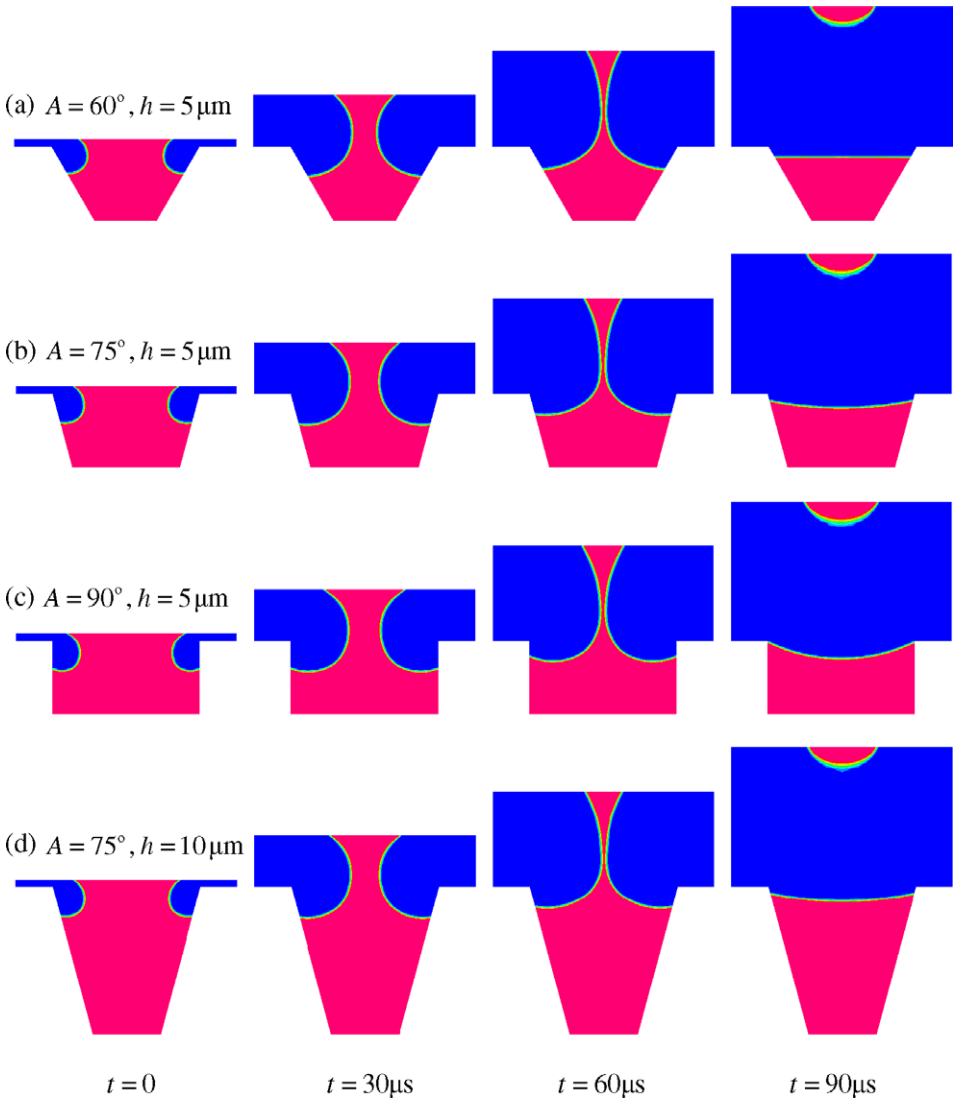

Fig. 18. Instantaneous contours of the volume fraction of the liquid between cavity and plate with $\beta = \gamma = 60°$ and $c_o = 0.5$ μm.

3.2.3. Effect of initial distance

In the real printing process, the upper pad is pressed tightly against the gravure plate before separation. In numerical modeling, however, the geometry is singular if the plate and the cavity are initially in contact. Hence, in our simulations, the cavity and the plate are initially separated by a distance c_o. Here we select different initial distances and compare the results with those obtained using the value employed in the above simulations, $c_o = 1.0$ μm. Fig. 17 shows time histories of w_t and h_c with $\beta = \gamma = 60°$ for $c_o = 0.5$ μm, 1.0 μm and 1.5 μm. The curves for all c_o systems have similar shapes, but the curve for small c_o lags that for large c_o. The lag time is approximately that required for the upper plate to move from the small c_o to the large c_o. Since the capillary number is much smaller than 1, the results are close to the quasistatic solutions and the influence of the initial distance c_o is not significant. However, the results for smaller c_o deviate from the quasistatic solutions to a greater degree. As shown in Fig. 17, both w_t and h_c are slightly increased at the end of the transfer process as c_o increases.

3.2.4. Effect of cavity shape

Since the cavity opening width is kept unchanged, the cavity volume is increased if the incline angle A increases. Hence, we expect that more liquid will be transferred to the upper plate for systems with larger A. Simulations with $A = 60°$, 75° and 90° are carried out for comparison, and the instantaneous contours of the volume fraction ϕ are plotted in Fig. 18a–c. We fix the contact angles at $\beta = \gamma = 60°$ and the initial distance at $c_o = 0.5$ μm for all cases. The volume of the liquid V_o for $A = 60°$ is kept the same as in the simulations above, while for $A = 75°$ and 90° the volume of a trapezoid with the same height as that of $A = 60°$ (Fig. 12b) is used, as given in Table 4. As shown in Fig. 18a–c, at $t = 0$ the liquid width on the upper plate is wider for larger A since the two cavity side walls are more separated. As the plate moves upward, the stretching, breaking and recoil of the liquid are similar for

Table 4
Comparison of the total volume of liquid, the transferred volume and the transfer ratio for different cavity shapes

	Total volume (μm^2)	Transferred volume (μm^2)	Transfer ratio (%)
$A = 60°$, $h = 5$ μm	32.01	3.86	12.06
$A = 75°$, $h = 5$ μm	39.73	4.53	11.40
$A = 90°$, $h = 5$ μm	46.40	5.24	11.29
$A = 75°$, $h = 10$ μm	69.60	4.54	6.52

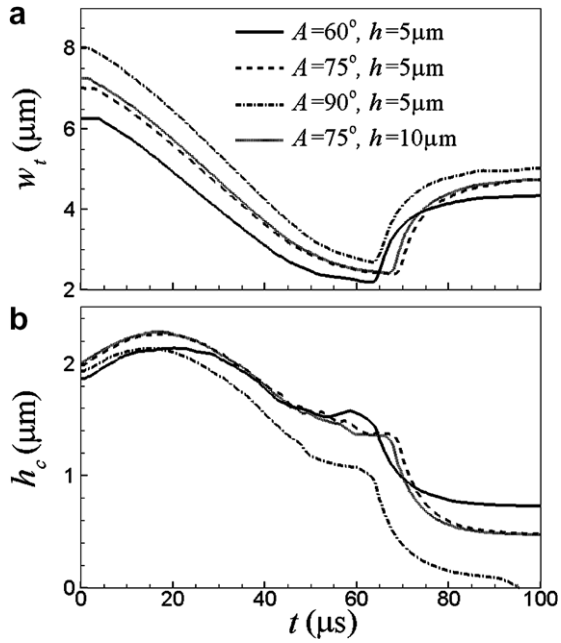

Fig. 19. Time histories of the width of liquid on the upper plate (a) and the cut height (b) with $\beta = \gamma = 60°$ and $c_o = 0.5$ μm for different incline angle A and depth h.

$A = 60°$, 75° and 90°. Time histories of the width w_t and the cut height h_c, plotted in Fig. 19, show that w_t increases with increasing A but the rate of increase with A becomes smaller at the end of the transfer process, while h_c is similar for each case at the initial stage but decreases more for larger A toward the end of the transfer process. As a result, the volume of transferred liquid increases with increasing A, but the transfer ratio decreases slightly due to the increase of the total volume (see Table 4).

The effect of the cavity depth is also taken into account here. The cavity with $A = 75°$ but the greater depth of $h = 10$ μm is used in the simulation, as shown in Fig. 18d. The liquid patterns during the transfer process are almost the same as those of the system with $h = 5$ μm, indicating that the liquid in the bottom of the cavity has negligible influence on the liquid transfer. Fig. 19 also shows that time histories of w_t and h_c for the $h = 10$ μm system coincide well with those of the system with $h = 5$ μm. Since the transferred volume of liquid is not increased by increasing the cavity depth, the transfer ratio is lower due to the higher total volume of the $h = 10$ μm cavity, as seen in Table 4. In other words, for the deeper cavity, more residual liquid remains within the cavity, which may cause the quality to deteriorate during repeated printing. Thus, in manufacturing the cavity depth should be as small as possible, while remaining greater than the maximum cut height.

To produce fine conductor lines in manufacturing electronics, a groove-patterned gravure plate is used for printing, where the present two-dimensional assumption is feasible. However, for a complex pattern holes are also presented in the gravure plate. Hence, we applied the axisymmetric condition in our simulations to examine the geometrical effects. Fig. 20 presents the final width of transferred liquid w_t and the maximum cut height h_c for both symmetric and axisymmetric conditions. It is shown that both w_t and h_c are decreased for the axisymmetric condition, and the difference is increased as β increases for a fixed γ. As compared with the symmetrical results of liquid transfer between two parallel plates (see Fig. 7), the transfer ratio is increased for $\alpha < \beta$ and is decreased for $\alpha > \beta$ in the axisymmetric case, where the surface tension has a more prominent influence on the transfer process. For liquid transfer between a cavity and a plate, it was observed in Fig. 14 that the contact line on the cavity side wall is difficult to

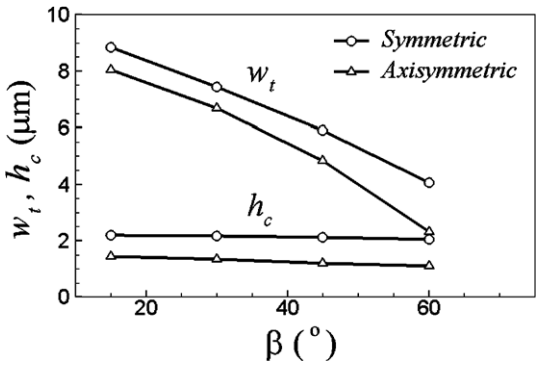

Fig. 20. Variations of the final width of liquid on the upper plate and the maximum cut height with $\gamma = 60°$ and different β. The axisymmetric results are compared with the symmetric ones.

move like that on a flat plate with a small contact angle. As a result, the transfer ratio is expected to be within the $\alpha > \beta$ region of plate to plate transfer as shown in Fig. 7. This conjecture is supported by the results in Fig. 20.

4. Summary and discussion

In the present study, we have proposed a numerical model for simulating liquid transfer during the micro-gravure-offset printing process. In particular, the printing of ink from the offset pad onto the substrate was modeled by liquid transfer between two parallel separating plates, and the picking up of ink from the gravure plate by the offset pad was modeled by liquid transfer between a trapezoidal cavity and an upward moving plate. The finite volume method was employed to discretize the continuity and momentum equations and grid deformation technology was adopted for the moving boundary. The VOF method was used to simulate the free surface between the liquid and the ambient air, so the whole problem was solved on a structured grid system.

For liquid transfer between two parallel plates, the stretching, breaking and recoil of the liquid were observed. During the breakup process, a satellite droplet was generated. Effects of the separation velocity, the liquid viscosity, the surface tension, the liquid size and the gravity force on the liquid transfer were estimated. Increasing the separation velocity or the liquid viscosity, or decreasing the surface tension, leads to a decrease of the transfer ratio for small contact angles at the target plate, but has the opposite effect for large contact angles at the target plate. It was found that the transfer ratio deviated from the theoretical quasistatic solution as the capillary number increased. An examination of the effects of the contact angles revealed that the width of the liquid transferred decreased as the contact angle at the upper plate increased or that at the bottom plate decreased. Although in the present simulations the surface property was only represented by contact angle, we have to mention that other important physic-chemical properties should be taken into account for reality and are difficult to model, such as the surface absorbance which makes it possible for 100% transfer (Pudas et al., 2002). Furthermore, we considered the non-Newtonian rheology of conductor ink and a shear-thinning fluid was simulated. The results showed a much faster breakup process due to the shear-thinning effect. Beside of this, most inks display viscoelastic behaviors which may affect the transfer process significantly (Yu et al., 2007).

The transfer process from the cavity to the upward moving plate can be divided into three stages: (1) a whole stretching stage; (2) a central stretching, breakup and recoil stage; and (3) an equilibrium stage. The effects of the contact angles on the final width of transferred liquid and the maximum cut height were examined.

The final width of the transferred liquid decreased as the contact angle at the upper plate increased, but varied only slightly for different contact angles at the cavity side wall. On the contrary, the cut height increased as the contact angle at the cavity side wall increased, but showed only a weak dependence on the contact angle at the upper plate. We additionally showed that as the cavity incline angle increased, the transferred liquid was increased, while the transfer ratio was slightly decreased due to the increased total volume at large incline angle. The axisymmetric condition was also examined, where the surface tension played a more prominent role as compared with the symmetric case. As a result, the transferred liquid was usually decreased since the liquid on the inclined cavity side wall behaved like that on a flat plate with a small contact angle. The initial distance between the cavity and the plate was shown to have only a small influence on the transfer process due to the small capillary number. In the practical printing, the soft pad is pressed tightly against the gravure plate and a high impression pressure plays a significant role in improving the transfer ratio. However, such effects cannot be modeled in the present numerical simulation. On the other hand, both the impression pressure and wall deformation can be tackled using the lubrication theory (Yin and Kumar, 2005), while other properties like contact angle and surface tension were neglected. It is desirable to formulate the impression pressure and wall deformation based on the full Navier–Stokes solver in our future work.

Acknowledgement

This work was supported by the Acceleration Research of the Korea Science and Engineering Foundation.

References

Brackbill, J.U., Kothe, D.B., Zemach, C., 1992. A continuum method for modeling surface tension. J. Comput. Phys. 100, 335–354.
Brakke, K.A., 1992. The surface evolver. Exp. Math. 1 (2).
Darhuber, A.A., Miller, S.M., Troian, S.M., Wagner, S., 2000. Process simulation for contact print microlithography. In: Technical Proceedings of the 2000 International Conference on Modeling and Simulation of Microsystems (Chapter 2).
Elsayad, S., Morsy, F., El-Sherbiny, S., Abdou, E., 2002. Some factors affecting ink transfer in gravure printing. Pigm. Resin Technol. 31 (4), 234–240.
Gillett, E.K. et al., 1991. Gravure Process and Technology. Gravure Association of America, Gravure Education Foundation.
Hagberg, J., Pudas, M., Leppävuori, S., Elsey, K., Logan, A., 2001. Gravure offset printing development for fine line thick film circuits. Microelectron. Int. 18, 32–35.
Hirt, C.W., Nichols, B.D., 1981. Volume of fluid (VOF) method for the dynamics of free boundaries. J. Comput. Phys. 39, 201–225.
Kennedy, P.K., 1995. Flow Analysis of Injection Molds. Hanser, Munich.
Lahti, M., Leppävuori, S., Lantto, V., 1999. Gravure-offset-printing technique for the fabrication of solid films. Appl. Surf. Sci. 142, 367–370.
Mikami, Y. et al., 1994. A new patterning process concept for large-area transistor circuit fabrication without using an optical mask aligner. IEEE Trans. Electron Dev. 41 (3), 306–314.
Peregrine, D.H., Shoker, G., Symon, A., 1990. The bifurcation of liquid bridges. J. Fluid Mech. 212, 25–39.
Pericc, M., Kessler, R., Scheuerer, G., 1988. Comparison of finite-volume numerical methods with staggered and collocated grids. Comput. Fluids 16, 389–403.
Powell, C.A., Savage, M.D., Guthrie, J.T., 2002. Computational simulation of the printing of Newtonian liquid from a trapezoidal cavity. Int. J. Numer. Methods Heat Fluid Flow 12 (4), 338–355.
Pudas, M., 2004. Gravure-offset Printing in the Manufacture of Ultra-fine-line Thick-films for Electronics. Oulu University Press.
Pudas, M., Hagberg, J., Leppävuori, S., 2002. The absorption ink transfer mechanism of gravure offset printing for electronic circuitry. IEEE Trans Electron. Packag. Manuf. 25 (4), 335–343.
Pudas, M., Hagberg, J., Leppävuori, S., 2004. Printing parameters and ink components affecting ultra-fine-line gravure-offset printing for electronics applications. J. Eur. Ceram. Soc. 24, 2943–2950.
Rider, W.J., Kothe, D.B., 1998. Reconstructing volume tracking. J. Comput. Phys. 141, 112–152.
Scardovelli, R., Zaleski, S., 1999. Direct numerical simulation of free-surface and interfacial flow. Annu. Rev. Fluid Mech. 31, 567–603.
Schwartz, L.W., 2002. Numerical modeling of liquid withdrawal from gravure cavities in coating operations; the effect of cell pattern. J. Eng. Math. 42, 243–253.
Schwartz, L.W., Moussalli, P., Campbell, P., Eley, R.R., 1998. Numerical modeling of liquid withdrawal from gravure cavities in coating operations. Trans. IChemE 76A, 22–29.
Van Doormaal, J.P., Raithby, G.D., 1984. Enhancements of the SIMPLE method for predicting incompressible fluid flows. Numer. Heat Transfer A – Appl. 7, 147–163.
Wilkes, E.D., Phillips, S.D., Basaran, O.A., 1999. Computational and experimental analysis of dynamics of drop formation. Phys. Fluids 11, 3577–3598.
Yin, X., Kumar, S., 2005. Lubrication flow between a cavity and a flexible wall. Phys. Fluids 17, 063101.
Yu, J.-D., Sakai, S., Sethian, J.A., 2007. Two-phase viscoelastic jetting. J. Comput. Phys. 220, 568–585.
Zhang, X., 1999. Dynamics of drop formation in viscous flows. Chem. Eng. Sci. 54, 1759–1774.